Detailed modeling of hydrodynamics, mass transfer and chemical reactions in a bubble column using a discrete bubble model

D. Darmana, N.G. Deen*, J.A.M. Kuipers

Fundamentals of Chemical Reaction Engineering, Faculty of Science and Technology, University of Twente, P.O. Box 217, 7500 AE Enschede, The Netherlands

Abstract

A 3D discrete bubble model is adopted to investigate complex behavior involving hydrodynamics, mass transfer and chemical reactions in a gas–liquid bubble column reactor. In this model a continuum description is adopted for the liquid phase and additionally each individual bubble is tracked in a Lagrangian framework, while accounting for bubble–bubble and bubble–wall interactions via an encounter model. The mass transfer rate is calculated for each individual bubble using a surface renewal model accounting for the instantaneous and local properties of the liquid phase in its vicinity. The distributions in space of chemical species residing in the liquid phase are computed from the coupled species balances considering the mass transfer from bubbles and reactions between the species. The model has been applied to simulate chemisorption of CO_2 bubbles in NaOH solutions. Our results show that apart from hydrodynamics behavior, the model is able to predict the bubble size distribution as well as temporal and spatial variations of each chemical species involved.
© 2005 Elsevier Ltd. All rights reserved.

Keywords: Bubble column; Discrete bubble model; Mass transfer; Chemical reactions; CFD

1. Introduction

Bubble columns are used in a variety of industrial processes including large-scale production of base chemicals and synthetic fuels. Many processes involve gas–liquid mass transfer with accompanying reactions between the gas and the liquid phase itself or with components dissolved or suspended in it. Despite the widespread application of bubble columns and substantial research efforts devoted to understand their behavior, detailed knowledge on the fluid flow, mass transfer and chemical reactions as well as their interactions are still lacking.

The coupling between these phenomena is illustrated in Fig. 1. The chemical reaction rate depends on the local availability of the species which is determined by the interphase mass transfer process and the mixing induced by the bubbles.

The interphase mass transfer depends on the mass transfer coefficient, the specific interfacial area and chemical reaction rate. The mass transfer parameters are a function of the local prevailing hydrodynamics (Cents et al., 2003), which in its turn are affected by the bubble behavior and variation of physical properties due to inhomogeneous chemical species distributions. It is these complex interactions that makes the overall prediction of performance and scale-up of this type of reactor very difficult.

In recent years, computational fluid dynamics (CFD) has emerged as a powerful tool for both scientists and engineers. CFD modelling of dispersed gas–liquid two-phase flows has shown remarkable progress over the last decade. Two models are widely used for describing hydrodynamics of bubble columns, i.e. the Euler–Euler (E–E) model and Euler–Lagrange (E–L) model. The E–E model employs the volume-averaged mass and momentum conservation equations to describe the time-dependent motion of both phases (Deen et al., 2001; Sokolichin and Eigenberger, 1994;

* Corresponding author. Tel.: +31 53 489 4138; fax: +31 53 489 2882.
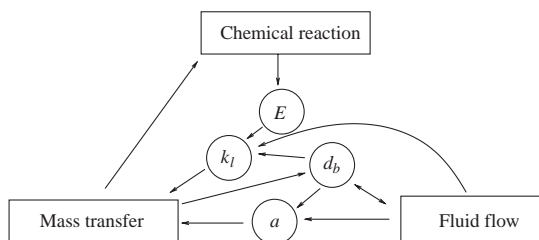*E-mail address:* n.g.deen@utwente.nl (N.G. Deen).

Fig. 1. Inter-dependency diagram of fluid flow, mass transfer and chemical reaction.

Pan and Dudukovic, 2000). The number of bubbles present in a computational cell is represented by a volume fraction and the information of the bubble size distribution is often obtained by incorporating population balance equations which take into account break-up and coalescence of bubbles as well as growth or shrinkage of bubbles as a consequence of mass transfer. The E–L model, on the other hand, adopts a continuum description for the liquid phase and additionally tracks each individual bubble using Newtonian equations of motion. This allows for a direct consideration of additional effects related to bubble–bubble and bubble–liquid interaction. Mass transfer with and without chemical reaction, bubble coalescence and re-dispersion can be incorporated directly (Tomiyama et al., 1997; Delnoij et al., 1997; Sokolichin and Eigenberger, 1994). Unlike the E–E model, the E–L model does not require additional models to predict the bubble size distribution since this information is already part of the solution. A drawback of the E–L model compared to the E–E model is its limitation on the number of bubbles that can be handled (i.e. less than $O(10^5)$) since for each individual bubble one equation of motion needs to be solved. This makes this method less attractive in handling large scale bubble columns.

Based on the E–E model, Fleischer et al. (1996) have pioneered to combine hydrodynamics, mass transfer and chemical reactions into a one-dimensional plug flow model accounting for axial dispersion and heat effects. The model consists of a liquid mass balance for each chemical species involved and momentum and energy balances for the liquid phase. The mass transfer rate is calculated from the two film theory based on the bubble size predicted by a population balance model. This model has been used to predict transient behavior of chemisorption of carbon dioxide into an aqueous solution of sodium hydroxide in a gas-lift reactor. A similar method was used by Márquez et al. (1999a,b) to study the coupling between hydrodynamics and chemical reaction without mass transfer in an external-loop gas liquid reactor. This model also has been adopted in several CFD software packages, which are used to solve a wide variety of practical two phase problems (Al-Rashed and Jones, 1999; Buwa and Ranade, 2002; Ranade and Tayalia, 2001).

The model of Fleischer is able to qualitatively predict the transient behavior of a chemisorption process in a slender cylindrical bubble column. However, for more general ge-

ometries, experimental investigations by Becker et al. (1994) and Chen et al. (1994) indicate that bubble columns generally show an unsteady flow with considerable spatial variation of the key hydrodynamic quantities. Numerical simulations reported by Delnoij et al. (1999), Sokolichin and Eigenberger (1994) and Deen et al. (2001) also show that unsteady vortical structures appear in 2D and 3D simulations. These results suggest that a 1D plug flow model as was used in Fleischers model is not able to capture the unsteady hydrodynamics behavior of a bubble column.

In this paper we present a detailed 3D model for the hydrodynamics, mass transfer and chemical reactions in an isothermal bubble column operated in the homogeneous regime. The E–L model is adopted to solve the hydrodynamics since incorporation of the bubble size distribution and interphase mass transfer calculation is relatively straightforward. The model is applied to study the coupling of hydrodynamics, gas–liquid mass transfer and chemical reactions in a square bubble column. First we will focus on the hydrodynamics of the column and compare our results with experimental and numerical results obtained by Deen et al. (2001). The mixing characteristics of the column will subsequently be studied with the use of hydrodynamics and species tracking models. Next the physical absorption of CO_2 into water will be addressed and finally the complete model will be used to investigate chemisorption of CO_2 bubbles into an aqueous solution of sodium hydroxide.

2. Model formulation

The three-dimensional model described in this paper is an extension of the hydrodynamic E–L model of Delnoij et al., 1999, which is applicable to disperse (homogeneous) regimes, which are characterized by low gas velocities and relatively small spherical bubbles that do not coalesce nor break-up. The interphase mass transfer is calculated for each bubble using the surface renewal theory which takes into account both physical and chemically enhanced mass transfer. The spatial distributions of chemical species residing in the liquid phase are computed from the coupled species conservation equations formulatedd in the Eulerian framework. Moreover, the numerical implementation of direct bubble–bubble interaction and the two-way coupling between phases will be addressed in Section 3.

2.1. Bubble dynamics

The motion of for each individual bubble is computed from the bubble mass and momentum equations. The liquid phase contributions are taken into account by the interphase mass transfer rate $\dot{m}$ and the net force $\sum F$ experienced by each individual bubble. For an incompressible bubble, the equations can be written as

$$\rho_b \frac{d(V_b)}{dt} = (\dot{m}_{l \to b} - \dot{m}_{b \to l}), \qquad (1)$$

Table 1
Overview of forces acting on a bubble

Force	Closure
$\mathbf{F}_G = \rho_b V_b \mathbf{g}$	—
$\mathbf{F}_P = -V_b \nabla P$	—
$\mathbf{F}_D = -\frac{1}{2} C_D \rho_l \pi R_b^2 \|\mathbf{v} - \mathbf{u}\|(\mathbf{v} - \mathbf{u})$	$C_D = \frac{2}{3}\sqrt{E\ddot{o}}$
$\mathbf{F}_L = -C_L \rho_l V_b (\mathbf{v} - \mathbf{u}) \times \nabla \times \mathbf{u}$	$C_L = 0.5$
$\mathbf{F}_{VM} = -C_{VM} \rho_l V_b \left(\frac{D_b \mathbf{v}}{D_b t} - \frac{D_l \mathbf{u}}{D_l t} \right)$	$C_{VM} = 0.5$

$$\rho_b V_b \frac{d\mathbf{v}}{dt} = \sum \mathbf{F} - \left(\rho_b \frac{dV_b}{dt} \right) \mathbf{v}. \tag{2}$$

The interphase mass transfer term $\dot{m}$ is calculated using a method, which will be describe in Section 2.4. The net force acting on each individual bubble is calculated by considering all the relevant forces. It is composed of separate, uncoupled contributions such as: gravity, pressure, drag, lift and virtual mass

$$\sum \mathbf{F} = \mathbf{F}_G + \mathbf{F}_P + \mathbf{F}_D + \mathbf{F}_L + \mathbf{F}_{VM}. \tag{3}$$

Expressions for each of these forces can be found in Table 1 (see Delnoij et al., 1997 for a discussion on the forces experienced by a bubble). Note that the closure models used in this article is for model demonstration only, more sophisticated closure models may be used to obtain better results.

2.2. Liquid phase hydrodynamics

The liquid phase hydrodynamics is represented by the volume-averaged Navier–Stokes equation, which consists of continuity and momentum equations. The presence of bubbles is reflected by the liquid phase volume fraction ε_l, the source term that accounts for the interphase mass transfer $\dot{M}$, and the total interphase momentum transfer due to forces and mass transfer Φ

$$\frac{\partial}{\partial t}(\varepsilon_l \rho_l) + \nabla \cdot \varepsilon_l \rho_l \mathbf{u} = (\dot{M}_{b \to l} - \dot{M}_{l \to b}), \tag{4}$$

$$\frac{\partial}{\partial t}(\varepsilon_l \rho_l \mathbf{u}) + \nabla \cdot \varepsilon_l \rho_l \mathbf{u}\mathbf{u} = -\varepsilon_l \nabla P - \nabla \cdot \varepsilon_l \tau_l + \varepsilon_l \rho_l \mathbf{g} + \Phi. \tag{5}$$

The liquid phase flow is assumed to be Newtonian, thus the stress tensor τ_l can be represented as

$$\tau_l = -\mu_{\text{eff},l}[((\nabla \mathbf{u}) + (\nabla \mathbf{u})^T) - \frac{2}{3}\mathbf{I}(\nabla \cdot \mathbf{u})], \tag{6}$$

where $\mu_{\text{eff},l}$ is the effective viscosity. In the present model the effective viscosity is composed of two contributions, the molecular viscosity and the turbulent viscosity

$$\mu_{\text{eff},l} = \mu_{L,l} + \mu_{T,l}. \tag{7}$$

Deen et al. (2001) did extensive work on the implementation and verification of a model that could account for the sub-grid scale turbulence. They concluded that the large

eddy simulation (LES) turbulence model implemented in the E–E framework outperforms the k–ε model in predicting the experimentally observed dynamic behavior of the flow in a square bubble column. Recently van den Hengel et al. (2003) and Láin and Sommerfeld (2004) have successfully employed LES in combination with the E–L model and obtained good agreement with experimental data in a square and cylindrical bubble column. Following them, the turbulent viscosity $\mu_{T,l}$ represents the contribution of the sub-grid scales. In the present study $\mu_{T,l}$ is described by the Smagorinsky (1963) model, which is expressed as

$$\mu_{T,l} = \rho_l (C_S \triangle)^2 |\mathbf{S}|, \tag{8}$$

where C_S is a model constant with a typical value of 0.1, $\mathbf{S}$ the characteristic filtered strain rate and $\triangle = (V_{\text{cell}})^{1/3}$ the SGS length scale.

2.3. Chemical species

The fraction of a chemical species j in the liquid mixture is represented by mass fraction Y_l^j. The presence of various chemical species are modeled through a transport equation for each species given by

$$\frac{\partial}{\partial t}(\varepsilon_l \rho_l Y_l^j) + \nabla (\varepsilon_l (\rho_l \mathbf{u}_l Y_l^j - \Gamma_{\text{eff}}^j \nabla Y_l^j))$$
$$= (\dot{M}_{b \to l} Y_b^j - \dot{M}_{l \to b} Y_l^j) + \varepsilon_l S^j, \tag{9}$$

where S^j is the source term accounting for production or consumption of species j due to homogeneous chemical reaction and

$$\Gamma_{\text{eff}}^j = \frac{\mu_{\text{eff},1}}{\text{Sc}^j}. \tag{10}$$

For a mixture, which consists of N_S chemical species, we only have to solve $N_S - 1$ transport equations represented by Eq. (9). The remaining species mass fraction can be calculated from the overall species balance using the following relation:

$$\sum_{j=1}^{N_S} Y_j = 1. \tag{11}$$

For a mixture consisting of N_S species, the liquid density and viscosity are taken as the average of properties of each species as follows

$$\frac{1}{\rho_l} = \sum_{j=1}^{N_S} \frac{Y_l^j}{\rho_l^j}, \tag{12}$$
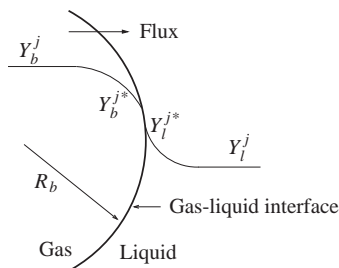
$$\mu_{L,l} = \sum_{j=1}^{N_S} Y_l^j \mu_l^j. \tag{13}$$

Fig. 2. Schematic representation of gas–liquid mass transfer.

2.4. Mass transfer

The interphase mass transfer in a bubble with radius R_b is considered to be driven by mass fraction gradients. The mass fraction of a chemical species j in the liquid phase and bubble are represented by Y_l^j and Y_b^j, respectively, while the value of both quantities at each side of the bubble–liquid interface is given by Y_l^{j*} and Y_b^{j*} (see Fig. 2).

The mass transfer in a bubble due to a mass fraction gradient of species j is represented as

$$\dot{m}_b^j = E k_l^j A_b \rho_l (Y_l^{j*} - Y_l^j), \tag{14}$$

where E is the enhancement factor due to chemical reactions, A_b is the surface area of the bubble and k_l^j is the mass transfer coefficient for species j, which is determined using a Sherwood relation for a moving bubble (Bird et al., 2002):

$$Sh = 2 + 0.6415(ReSc^j)^{1/2}. \tag{15}$$

When the mass transfer resistance lies in the liquid phase, the mass fraction on the liquid side of the interface can be determined using a Henry constant

$$Y_l^{j*} = H^j Y_b^j \frac{\rho_b}{\rho_l}, \tag{16}$$

where H^j is the Henry constant for the species j.

The total mass transfer rate is the sum of the mass transfer rates of all species j, thus

$$\dot{m}_b = \sum_{j=1}^{N_S} \dot{m}_b^j. \tag{17}$$

The mass transfer from the liquid to a bubble can be written as $\dot{m}_{l \to b} = \max(\dot{m}_b, 0)$, while the mass transfer from a bubble into the liquid is $\dot{m}_{b \to l} = \max(-\dot{m}_b, 0)$.

3. Numerical implementation

In this section the numerical implementation of the model described in Section 2 will be described briefly.

3.1. Time marching

To resolve the time-dependent motion of the bubbles and the liquid phase, as well as the chemical species, four different time scales are considered. The biggest time step (δt_{flow}) is employed in solving the Navier–Stokes equations to obtain the macroscopic liquid flow field. The interphase mass and momentum transfer are resolved on the scale of the bubble time step (δt_{bub}). To account for the possible encounters (collisions) between bubbles and the displacement of the bubbles an even smaller time step (δt_{ab}) is used. The chemical species transport equation is solved using a time step δt_{spec} similar to the δt_{flow}. However, for chemical species, which undergo fast chemical reactions a smaller time step is required, in order to prevent numerical instability.

3.2. Bubble tracking and direct bubble–bubble interaction

The mass and momentum conservation equation of the bubbles are ordinary differential equations. These equations are integrated numerically using a first-order explicit scheme. For a general time integrable variable ξ the formula can be written as

$$\xi^{t+1} = \xi^t + \left(\frac{d\xi}{dt}\right)^t \delta t_{\text{bub}}. \tag{18}$$

The mass and momentum balance equations for each bubble are solved sequentially. First, the mass transfer rate is calculated explicitly using the method describe in Section 2.4 to obtain the bubble volume rate of change. Using the numerical scheme described in Eq. (18), the bubble volume rate of change is integrated to obtain a new bubble size.

Subsequently the bubble momentum equation is solved by first calculating the interphase momentum and mass transfer term explicitly. The acceleration of each individual bubble is obtained in a straight forward manner using Eq. (2). The new bubble velocity is obtained by integrating the acceleration using Eq. (18).

The collision between bubbles is modeled using the so-called hard sphere model following the work of Hoomans et al. (1996). In this method a constant time step δt_{bub} is used to account for the forces acting on a bubble. Within this time step, the velocity of bubbles is assumed to change only due to binary collisions between the bubbles. A sequence of collisions is then processed, one collision at a time.

To predict the collision between bubbles, we extend the model that is widely used in the field of molecular dynamics (Allen and Tildesley, 1987) by taking into account the rate of change of the bubble size. Consider two bubbles, a and b, of radius R_a and R_b, respectively. At time t the bubbles are located at $\mathbf{r}_a$ and $\mathbf{r}_b$ with velocity $\mathbf{v}_a$ and $\mathbf{v}_b$ and bubble growth rates (in terms of bubble radius growth rate) $\dot{R}_a$ and $\dot{R}_b$. If those bubbles are to collide at time $t + \delta t_{ab}$ then the

following equation must be satisfied:

$$|\mathbf{r}_{ab}(t + \delta t_{ab})| = |\mathbf{r}_{ab} + \mathbf{v}_{ab}\delta t_{ab}|$$
$$= (R_a + R_b) + (\dot{R}_a + \dot{R}_b)\delta t_{ab}, \qquad (19)$$

where $\mathbf{r}_{ab} = \mathbf{r}_a - \mathbf{r}_b$ and $\mathbf{v}_{ab} = \mathbf{v}_a - \mathbf{v}_b$ and δt_{ab} is the time until the collision. The second and third term in Eq. (19) can be written in the quadratic equation in δt_{ab} as follows:

$$A\delta t_{ab}^2 + 2B\delta t_{ab} + C = 0 \qquad (20)$$

with

$$A = \mathbf{v}_{ab}^2 - (\dot{R}_a + \dot{R}_b)^2,$$
$$B = \mathbf{r}_{ab} \cdot \mathbf{v}_{ab} - (R_a + R_b)(\dot{R}_a + \dot{R}_b),$$
$$C = \mathbf{r}_{ab}^2 - (R_a + R_b)^2.$$

If $B > 0$ then the two bubbles are moving away from each other and they will not collide. Otherwise (if $B < 0$) there is a chance in a certain period that the bubbles will be collide. Provided that Eq. (20) has a positive discriminant, two positive roots will arise and the smaller will correspond to the impact:

$$\delta t_{ab} = \frac{-B - \sqrt{B^2 - AC}}{A}. \qquad (21)$$

In order to calculate the collision time efficiently we use the so-called bubble neighbor region. Only bubbles located inside this region are considered to be possible collision partners. Hoomans et al. (1996) and Delnoij et al. (1999) use a rectangular shape to represent the neighbor region, however in this work we choose a spherical shaped neighbor region since this shape is more natural with respect to the bubble shape. For all the bubbles inside the neighbor area of a certain bubble a (see Fig. 3), we calculate the collision time δt_{ab} between bubble a and the possible collision partner b using Eq. (20) . Note that the collision partner may also be one of the column walls or the top surface.

For all the possible collision pairs, the smallest δt_{ab} is selected. This δt_{ab} will be used to update both size and position of all bubbles. However for bubbles a and b, which correspond to the smallest δt_{ab}, a collision procedure is carried out and new velocities are determined.

A pair of colliding bubbles will bounce during the collision event. The velocities of both bubbles after the bounce are determined by splitting the initial velocities into a normal and tangential component with respect to the line connecting the centers of mass of both bubbles. The tangential component does not change due to a collision, while the new normal component is calculated from

$$v_{n,a}^{\text{aftercollision}} = 2\frac{m_a v_{n,a} + m_b v_{n,b}}{m_a + m_b} - v_{n,a}, \qquad (22)$$

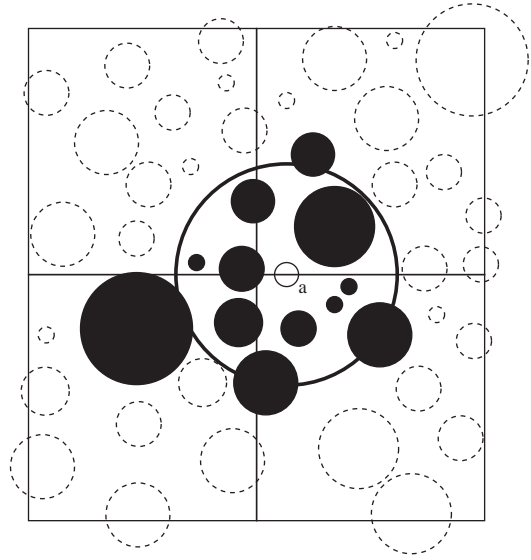where the new velocity of bubble b is calculated in a similar way.

Fig. 3. Area scanned for possible neighbors. Thick circle represent the neighbors boundary for bubble a. All bubble which has distance between its perimeter and bubble a perimeter smaller than the boundary perimeter belongs to this neighbors.

3.3. Liquid flow field

A finite difference technique was adopted to discretize the governing equations of the liquid phase. The volume-averaged Navier–Stokes equations have been solved with a semi-implicit method for pressure linked equations (SIMPLE-algorithm). A staggered grid is employed to prevent numerical instability. First-order explicit time differencing is applied for the time derivative. The convective terms of the mass and momentum conservation equations are treated implicitly using a second-order accurate Barton scheme (Centrella and Wilson, 1984). Moreover, the pressure gradient is treated implicitly, while the interphase mass and momentum transfer and all other terms are treated explicitly. The resulting set of linear equations yields a discretized pressure-Poisson equation, which is solved iteratively using the incomplete Choleski conjugate gradient (ICCG) method, which is incorporated in the PETSc library (Balay et al., 2001).

3.4. Chemical reactions and species transport equations

All the terms in the species transport equation are discretized using a fully implicit method, except for the interphase mass transfer and chemical reaction rate, which appear as source terms and are treated explicitly. The convective flux is treated using a first-order accurate upwind scheme which is corrected using deferred correction method (Ferziger and Peric, 1999) in order to be consistent with the second-order Barton scheme method, which is used in solving the Navier–Stokes equation. The resulting discretized equations for all species are solved simultaneously
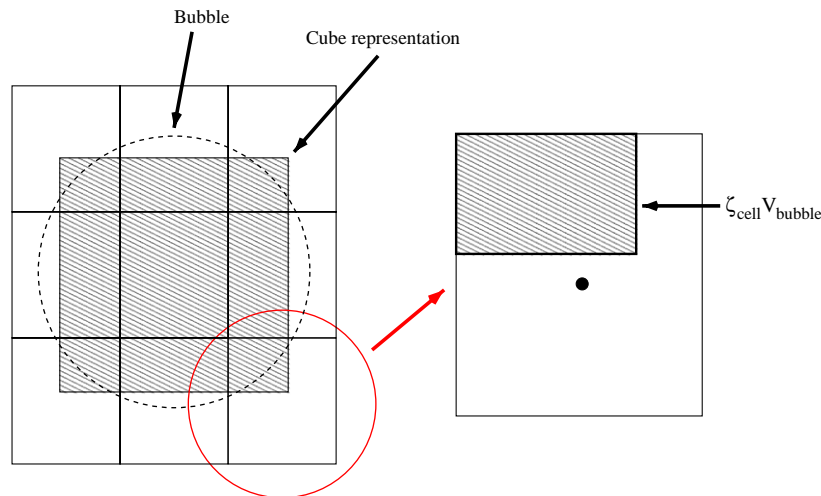
Fig. 4. Schematic representation of the porosity mapping technique.

using an algorithm similar to that used by Hjertager (1998) in solving the mass conservation equations in a multi-fluid model. Using this technique, the algebraic constraint for the species equation (Eq. (11)) is automatically imposed, yielding mass fractions for each species which are bounded between 0 and 1.

3.5. Interphase coupling

The coupling between the liquid phase and the bubbles is accomplished through the liquid phase volume fraction ε_l, the interphase momentum transfer rate Φ, as well as the mass transfer rate from and to the bubbles. Since the liquid phase and the bubbles are defined in different reference frames (i.e. Lagrangian and Eulerian), a mapping technique which correlates the two reference frames is required. This mapping technique translates the Lagrangian bubble quantities to the Eulerian grid, which are required as closure for the liquid phase equations and vice versa.

Most of the mapping techniques in literature are developed for bubbles, which are much smaller than the grid size (Delnoij et al., 1999; Tomiyama et al., 1997). However, in order to allow for changes in bubble size due to coalescence and mass transfer processes, it is desirable that bubbles can become larger than the computational grid size.

In this section we propose a new mapping technique, which allows us to simulate bubbles, which can be smaller as well as bigger than the Eulerian grid size.

3.5.1. Porosity mapping
The bubble volume fraction ε_b in a computational cell is calculated from the volume occupied by the bubbles present in the cell under consideration

$$\varepsilon_b = \frac{1}{V_{\text{cell}}} \sum_{\forall i \in \text{cell}} \zeta^i_{\text{cell}} V^i_b \tag{23}$$

with ζ^i_{cell} is the volume fraction of the ith bubble included in the cell under consideration.

The liquid volume fraction ε_l is calculated using the algebraic expression

$$\varepsilon_l = 1 - \varepsilon_b. \tag{24}$$

Eq. (23) requires a value ζ^i_{cell} which unfortunately depends on the shape of the bubbles. The prediction of the bubble shape is a tedious task, since it depends on various parameters such as fluid properties, bubble size and the time-dependent flow field around the bubble. Even for a simple shape such as a sphere or ellipsoid, the calculation of ζ^i_{cell} requires significant computational effort, especially if the size of bubble is larger than the size of the computational grid. For this reason, we use a cubic shape to represent the bubble following the work of Tomiyama et al. (1997) with the arguments: (1) the calculation of ζ^i_{cell} is easy and takes little CPU time; and (2) since the actual bubbles take time-dependent complex shapes, there may be little difference between the cubic approximation and other, more sophisticated approximations such as spherical and ellipsoidal shapes.

Fig. 4 shows how we can map portion of a bubble into the involved computational cells. Special attention should be given to cells, which are entirely occupied by a bubble and do not allow for the solution of the liquid phase conservation equations. To overcome this problem the liquid phase porosity has been forced to have the lowest value $\varepsilon_l = \varepsilon_{\text{low}}$. The value of ε_{low} that we choose will influence the accuracy as well as the computational cost to solve the problem. We found that by taking $\varepsilon_{\text{low}} = 0.05$ both aspects are treated in a satisfactory manner.

3.5.2. Lagrange to Euler mapping
In order to close Eqs. (4)–(9) a relation between a Lagrangian quantity of bubbles ω and the respective Eulerian value Ω is required. Since Ω is given as a volume-averaged
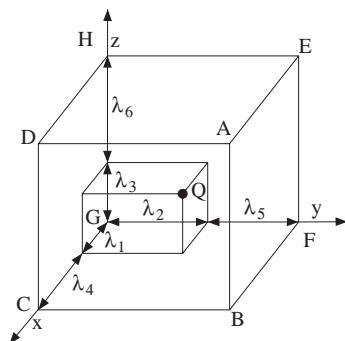
Fig. 5. Notation used for mapping Eulerian data at points A–H to Lagrangian point Q (after Tomiyama et al., 1997).

value of ω in a unit volume, let us consider a computational cell in $3-D$ Cartesian coordinates which has volume V_{cell}. For all bubbles i in this cell, the relation between ω and Ω can be written as

$$\Omega = \frac{1}{V_{\text{cell}}} \sum_{\forall i \in \text{cell}} \zeta_{\text{cell}}^i V_b^i \omega, \tag{25}$$

where ζ_{cell}^i is calculated with the cubic shape representation, which was introduced earlier.

3.5.3. Euler to Lagrange mapping

To evaluate forces experienced by each bubble, we need information of liquid quantities which are defined on the Eulerian grid. For this purpose we adopt the volume weighing method, which was used by Delnoij et al. (1999) and Tomiyama et al. (1997). As shown in Fig. 5, the value of any physical quantities Ω at point Q (denotes as ω) can be calculated as

$$\begin{aligned} \omega = {} & \lambda_1 \lambda_2 \lambda_3 \Omega_A + \lambda_1 \lambda_2 \lambda_6 \Omega_B + \lambda_1 \lambda_5 \lambda_6 \Omega_C \\ & + \lambda_1 \lambda_5 \lambda_3 \Omega_D + \lambda_4 \lambda_2 \lambda_3 \Omega_E + \lambda_4 \lambda_2 \lambda_6 \Omega_F \\ & + \lambda_4 \lambda_5 \lambda_6 \Omega_G + \lambda_4 \lambda_5 \lambda_3 \Omega_H, \end{aligned} \tag{26}$$

where $0 \leqslant \lambda_k \leqslant 1$ and $\lambda_1 + \lambda_4 = \lambda_2 + \lambda_5 = \lambda_3 + \lambda_6 = 1$.

3.6. Computational sequence

The complex phenomena involving hydrodynamics, mass transfer and chemical reactions are solved in a sequential manner. A diagram of the computational sequence is presented in Fig. 6. For every flow time step δt_{flow}, first, the interphase mass and momentum transfer are calculated explicitly for each individual bubble. The liquid quantities required to calculate these terms are obtained from the Euler to Lagrange mapping technique (Section 3.5.3). Using the interphase mass and momentum transfer, the bubbles size and position are updated taking into account direct bubble–bubble and bubble–wall interaction (Section 3.2).

The available bubble size and positions are mapped to the Eulerian mesh using the porosity mapping method (Section 3.5.1) to obtain the liquid phase porosity in ev-
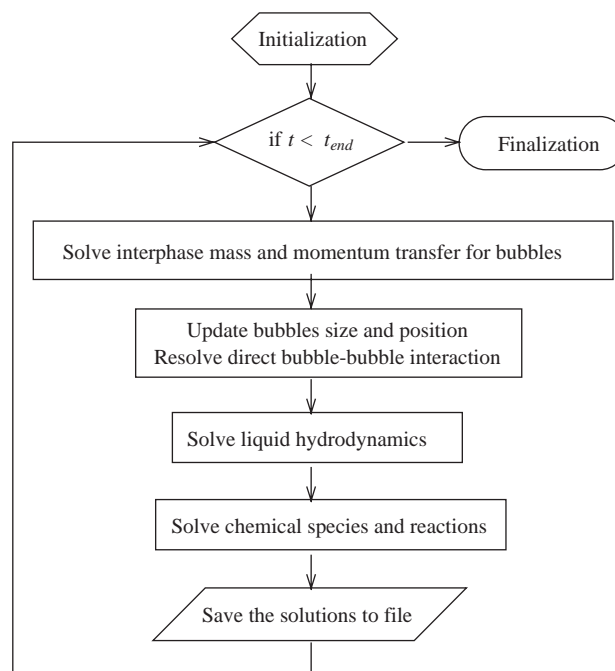

Fig. 6. Computational sequence diagram of the DBM.

ery Eulerian computational cell. The interphase mass and momentum transfer rate, which was previously calculated from every individual bubble is also mapped to the Eulerian cell using the Lagrangian to Eulerian mapping technique (Section 3.5.2). Using the new liquid porosity as well as the interphase mass and momentum transfer rate, the liquid hydrodynamics are solved to obtain the liquid phase hydrodynamics at the new time level (Section 3.3). Finally, the chemical reactions and species transport equation are solved to obtain a chemical species distribution at the new time level (Section 3.4). This sequential procedure is repeated until a specified simulation end time is reached.

4. Geometry and boundary condition

Deen et al. (2001) performed particle image velocimetry (PIV) measurements in a 3D bubble column filled with distilled water. The column has a square cross-section ($W \times D$) of $0.15 \times 0.15 \, \text{m}^2$ and a height (L) of $0.45 \, \text{m}$. Air with a superficial gas velocity of $4.9 \, \text{mm/s}$ was introduced into the system through a perforated plate. The plate contained 49 holes with a diameter of $1 \, \text{mm}$, which were positioned in the middle of the plate at a square pitch of $6.25 \, \text{mm}$.

The column is modeled using the DBM code, which was described in the preceding section. The computational grid consists of $30 \times 30 \times 90$ cells and the flow time step (δt_{flow}) is 1.0×10^{-3} s. Preliminary calculations revealed that this configuration gives a grid and time step independent solution. The boundary conditions are imposed to the column using the flag matrix concept of Kuipers et al. (1993) as can

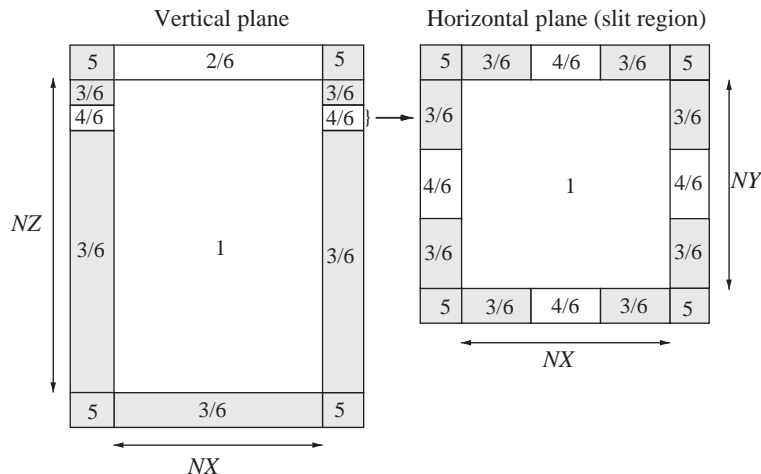Vertical plane   Horizontal plane (slit region)

Fig. 7. Typical boundary conditions used in simulations with the discrete bubble model. The vertical plane is at $j = NY/2$ while a slit is defined at $k = NZ - 1$.

Table 2
Cell flags and corresponding cell types used in defining boundary conditions

Flag	Boundary conditions
1	Interior cell, no boundary conditions specified
2	Impermeable wall, free slip boundary
3	Impermeable wall, no slip boundary
4	Prescribed pressure cell, free slip boundary
5	Corner cell, no boundary conditions specified
6	Neumann boundary for species transport equation ($\nabla Y^j \cdot \overrightarrow{n} = 0$)

be seen in Fig. 7. The definition of each boundary condition can be seen in Table 2. The configuration of boundary conditions used in the simulations has been carefully investigated. The prescribed pressure cells close to the column surface wall are required as inlet as well as outlet channel to compensate for the change of liquid volume due to bubbles entering and leaving the column. The width of this pressure cell slit is one third of the total width of the column and located in the middle. It was found that this configuration avoids hydrodynamic instabilities developing at the top surface of the column. Furthermore, for the species transport equations, a Neumann boundary condition is used in all of the boundary cells.

Each hole in the perforated plate is modeled as a position in the bottom of the column where bubbles with specific size enter the column with a fixed velocity. All the bubbles entering the column have a diameter of 4 mm as has been experimentally observed by Deen et al. (2001). The distance between the center of two consecutive bubbles released from a single hole δ_b is set to $2.5 \times R_b$. This arrangement is made to avoid unnecessary collisions between two consecutive bubbles immediately after they enter the column. The velocity of bubbles entering the column is determined from the superficial velocity through the following formula:

$$v_{z,\text{enter}} = \frac{v_s \delta_b W \times D}{N_h V_b} \tag{27}$$

with $\mathbf{v}_s$ the superficial gas velocity, $W \times D$ the cross sectional area of the column and N_h is number of holes.

For all of the holes, the vertical position of the bubbles underneath the bottom plate is generated in such way that none of the bubbles enters the column at the same time. This was implemented in order to prevent (artificial) pulsing behavior of the incoming bubbles, which would occur if bubbles enter the column through all holes simultaneously. By doing so, the occurrence of undesired pressure fluctuations at the top of the column was prevented.

When a bubble hits the top boundary of the column, the bubble is marked to be removed from the column. The removal procedure is very important since it can influence the overall flow inside the column and in some case may induce instabilities in the numerical solution. When a bubble is marked to be removed from the column, its velocity and interphase mass and momentum transfer to the liquid phase are no longer updated. The bubble is still however, moving with a constant velocity using the last velocity value calculated immediately before it touches the top boundary. Using this velocity, the bubble is passing the top boundary according to the normal bubble time step. The portion of bubble which still resides in the column is still accounted for in the calculation of the liquid phase volume fraction. When the entire bubble is completely above the top boundary, the bubble is disposed from the bubble list which concludes the bubble removal procedure.

For a typical bubble size used in the simulation, the whole process of removing a bubble takes around 10^{-2} s and within this interval the liquid phase gradually adapts the change in the volume fraction. Compared with the instantaneous bubble removing technique used by Delnoij et al. (1999),

the method presented here can eliminate numerical instabilities at the top boundary especially when removing a bubble which has bigger size than the computational grid cell.

5. Verification

To verify the method for calculating liquid phase porosity, the Lagrangian to Eulerian mapping as well as the Eulerian to Lagrangian mapping, we consider a case in which a bubble rises through a quiescent liquid. The terminal rise velocity of the bubble resulting from our simulations is compared with the analytical solution. For a bubble rising with a constant velocity through a quiescent liquid the buoyancy force equals the drag force. The drag coefficient is calculated based on Eötvös number as given in Table 1.

When the terminal rise velocity is reached the buoyancy force is equal to the drag force, hence the terminal rise velocity can be determined as

$$\mathbf{v}_{\text{terminal}} = \left(\frac{8(\rho_l - \rho_b) R_b \mathbf{g}}{3 C_D \rho_l} \right)^{1/2}$$
$$= \left(\frac{4 (\rho_l - \rho_b) \sigma \mathbf{g}}{\rho_l^2} \right)^{1/4}. \tag{28}$$

Using $\rho_l = 1000 \, \text{kg/m}^3$, $\rho_b = 1 \, \text{kg/m}^3$, $\mathbf{g} = 9.81 \, \text{m/s}^2$ and $\sigma = 0.073 \, \text{N/m}$ we obtain a terminal rise velocity of $0.2312 \, \text{m/s}$. Note that by calculating the drag coefficient using relation reported in Table 1, the terminal rise velocity of the bubble is independent of its size.

In the simulation, a bubble is released at the bottom of the column and because of the buoyancy, the bubble will start to rise. Simulations were conducted for bubble diameters of 4 and 10 mm, with computational cells of 5 and 10 mm.

The comparison between the analytical terminal rise velocity and the simulations are shown in Fig. 8. As we can see from this figure, the model can reproduce the terminal rise velocity accurately. For the 10 mm bubble however, the terminal rise velocity shows small wiggles. These (very small) wiggles can be attributed to the mapping technique and occur when the bubble crosses the face of a computational cell. The order of this wiggle however is very small compared to the magnitude of the terminal rise velocity, thus we can conclude that the proposed mapping method performs satisfactory and can be used for further simulations.

Another simulation was performed to verify the time integration procedure that has been implemented to track the bubble size as well as bubble mass due to mass transfer. The verification was carried out by simulating the rise of a single bubble with mass transfer. The mass transfer rate was set to be constant by selecting the initial conditions of the species Y_l^j, k_l and Y_l^{j*} in such a way that $k_l(Y_l^j - Y_l^{j*}) = 4 \times 10^{-6} \, \text{m/s}$. With this arrangement, the analytical solution
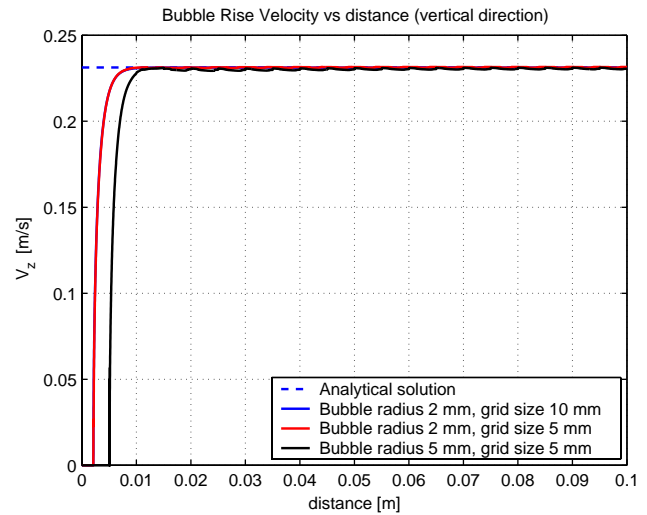

Fig. 8. Single air bubble rise velocity in an initially quiescent column filled with water. Several combinations of bubble and grid size as compared with the analytical solution.
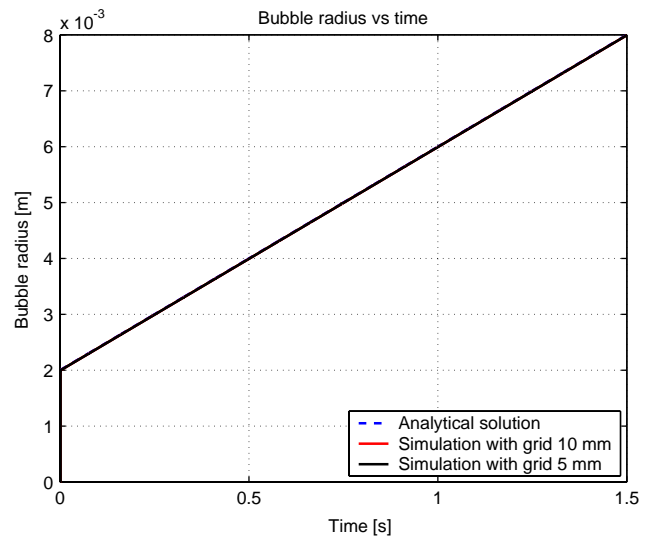

Fig. 9. Time integration verification of a single air bubble size rising in an initially quiescence water. Bubble initial diameter 4 mm; $k_l(Y_l^j - Y_l^{j*}) = 4 \times 10^{-6} \, \text{m/s}$. Simulation results with two different grid size practically coincide with the analytical solution.

of the bubble size becomes

$$R_b(t) = k_l \left(Y_l^j - Y_l^{j*} \right) \frac{\rho_l}{\rho_b} t + R_b(0). \tag{29}$$

A bubble with an initial diameter of 4 mm is released at the bottom of the column. The bubble size is tracked in time and the result is compared with the analytical solution. Fig. 9 shows the comparison of the analytical solution and single bubble simulation with grid sizes of 5 and 10 mm. This figure shows that the simulation results and the analytical solution practically coincide. These results verify that the time integration of the bubble size is correctly implemented and can be used for further simulations.
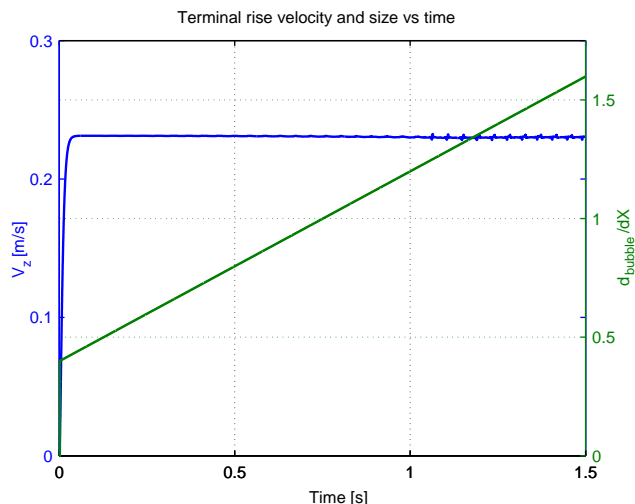
Fig. 10. Bubble terminal rise velocity for an air bubble experienced constant radius rate. Bubble initial diameter 4 mm; $k_l(Y_l^j - Y_l^{j*}) = 4 \times 10^{-6}$ m/s; grid size 10 mm.

As mentioned in the previous section, the terminal rise velocity is independent of the bubble size. This fact can also be observed in Fig. 10. As can be seen from this figure, after the bubble reaches its terminal velocity, the velocity remains constant, despite the fact that the bubble size is increasing. When the bubble diameter exceeds the size of the computational cell, small wiggles start to develop. However, the order of these wiggles is again very small and does not increase as the bubble size increases.

6. Results

In order to demonstrate the capabilities of the model four case studies are presented in this section. The square bubble column introduced in Section 4 is used as a base configuration. The hydrodynamics part of the model is compared with PIV measurements of Deen et al. (2001).

6.1. Hydrodynamics

In this case study, the hydrodynamics of an air–water system are investigated. The gas–liquid flow in a square bubble column is simulated using the hydrodynamic model as described in Section 2.1 and 2.2. Air is injected into an initially quiescent liquid as indicated in Fig. 11. Shortly after the bubbles are released into the column, a bubble plume rises through the column and creates a typical mushroom like shape. Due to the gas–liquid momentum coupling, some motion is induced in the liquid phase, and after a while the entire bulk liquid starts to move. The first bubbles escape from the column after 1.5 s simulations. After some time the motion inside the bubble becomes unstable. Strong circulation patterns appear with up flow in the center region and down flow in the corners of the column. Due to the liq-

uid down flow, some bubbles close to the wall are dragged downwards to the lower region of the column before being dragged again to the column surface by the upward flow.

The bubble plume is meandering in a random fashion. Using animation representation of our simulation results as suggested by Delnoij et al. (1997) we can see that this meandering behavior is due to random formation of vortices close to the column surface. The vortices generate strong down flow, which pushes the bubbles near the inlet region to one side when they reach the bottom of the column. The bubble plume will then move close to one side of the column. This process is repeated, but the vortex formation appears in another location, which will make the bubble plume move in another direction.

A time history plot of the vertical liquid velocity at one point in the column is shown in Fig. 12. As can be seen in this figure, the DBM simulation is able to reveal the highly dynamic nature of the bubble column hydrodynamics. As compared to the experimental measurements using laser Doppler anemometry (LDA) technique by Deen et al. (2001), the DBM results are in agreement for both time and velocity scales.

A more quantitative comparison with the experimental measurement is obtained through the long term (i.e. the statistical averaged) quantities. In the present study the time-averaged mean velocity and velocity fluctuations of the simulation are calculated during a 10–120 s interval. The mean velocity is calculated as follows:

$$\bar{\mathbf{u}} = \frac{1}{N_t} \sum_{i=1}^{N_t} \mathbf{u}_i, \tag{30}$$

where N_t is the number of time steps used in the averaging. The large scale velocity fluctuation is calculated as

$$\mathbf{u}' = \frac{1}{N_t} \sqrt{\sum_{i=1}^{N_t} (\mathbf{u}_i - \bar{\mathbf{u}})^2}. \tag{31}$$

The time averaged quantities are compared with the PIV measurements of Deen et al. (2001), who also conducted two fluid simulations of this column with a two fluid model using the commercial CFD package CFX. Fig. 13 shows the profile of the average liquid velocity in the vertical direction while the liquid phase vertical and horizontal velocity fluctuations can be seen in Fig. 14. As can be seen in these figures, the simulation results show good agreement with the experimental data. The average velocity profile gives a maximum value in the center of the column and a negative value close to the wall, which resembles a liquid flow pattern with liquid up-flow in the center region of the column and down flow near the walls.

Compared to the PIV measurements, the DBM simulations generally slightly overpredict the average and fluctuation velocities in the center region of the column, while the two-fluid simulations shows the opposite tendency. The vertical velocity fluctuations, measured with PIV, show a local
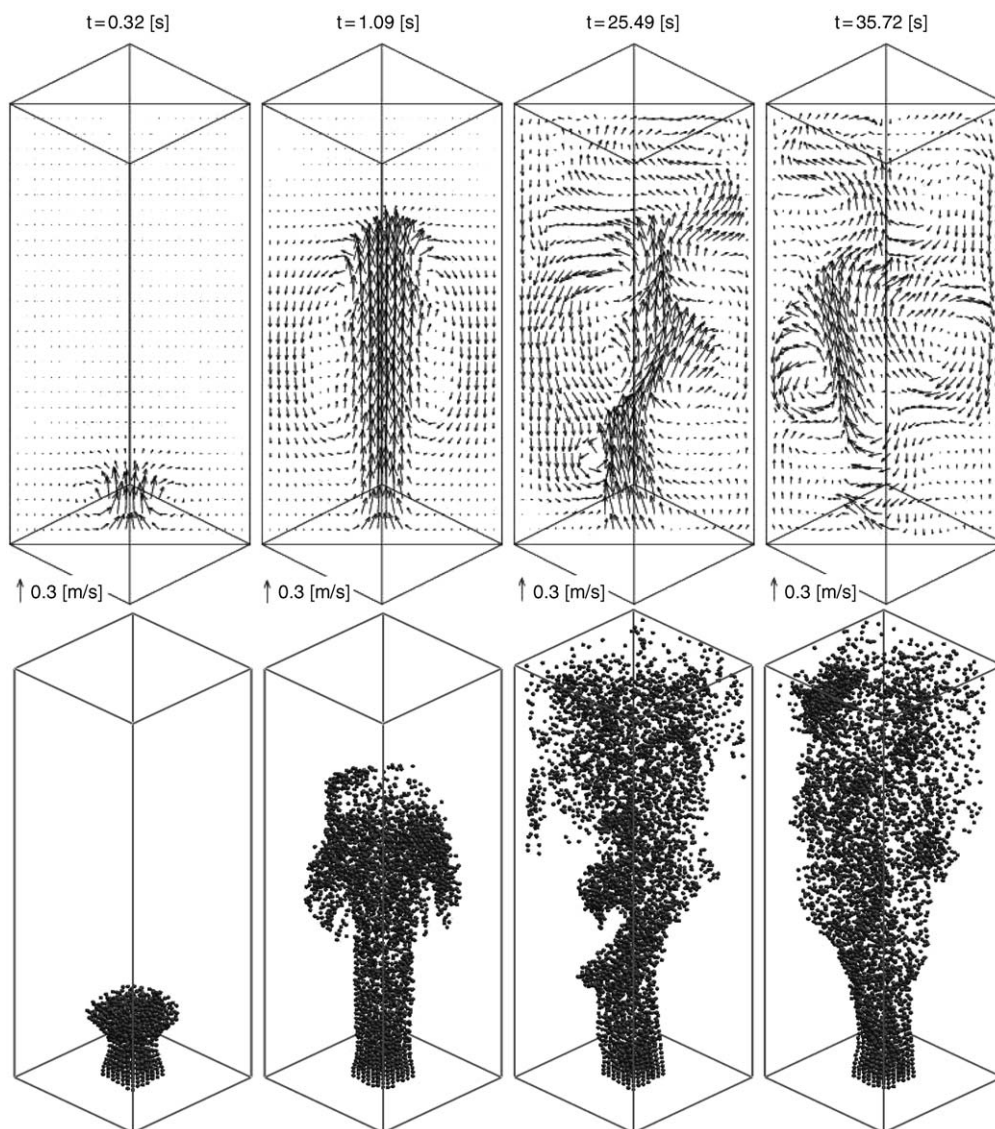
Fig. 11. Series of corresponding velocity fields and bubble position obtained from simulation of air–water bubble column at different time after the air was switched on. Gas superficial velocity = 4.9 mm/s.

minimum in the middle, which is also predicted nicely in the DBM simulation. The velocity fluctuations predicted by the two fluid model, however, do not show this feature.

6.2. Mixing

The liquid velocity induced by the motion of the bubbles generates mixing in the bubble column. The characteristics of the mixing is very important, since it will determine the homogeneity of chemical species present in the reactor. The mixing rate is normally determined by injecting a pulse of tracer containing a specified amount of tracer and by monitoring tracer concentrations within the reactor at single or multiple points (Ranade and Tayalia, 2001).

In the present study, the mixing mechanism of the air–water bubble column system is investigated immediately

after bubbles are injected by making use of three different tracers. The column is divided into three equal regions in the vertical direction. Initially, only one tracer is present in each region as can be seen in Fig. 15. The tracer is treated as a passive scalar, which is described by Eq. (9), where the source terms are all set to zero.

Fig. 16 shows the mixing sequence immediately after bubbles are introduced into the column. As can be seen, the tracers that are initially separated are pushed upward in the center region of column, because of the bubble motion. This upward motion is balanced by downward motion close to the column wall. The tracers, which come from the three regions then hit the top and bottom part of the column. The vortices present in these regions mix the tracers even further. The process is continued until all the tracer is mixed evenly.
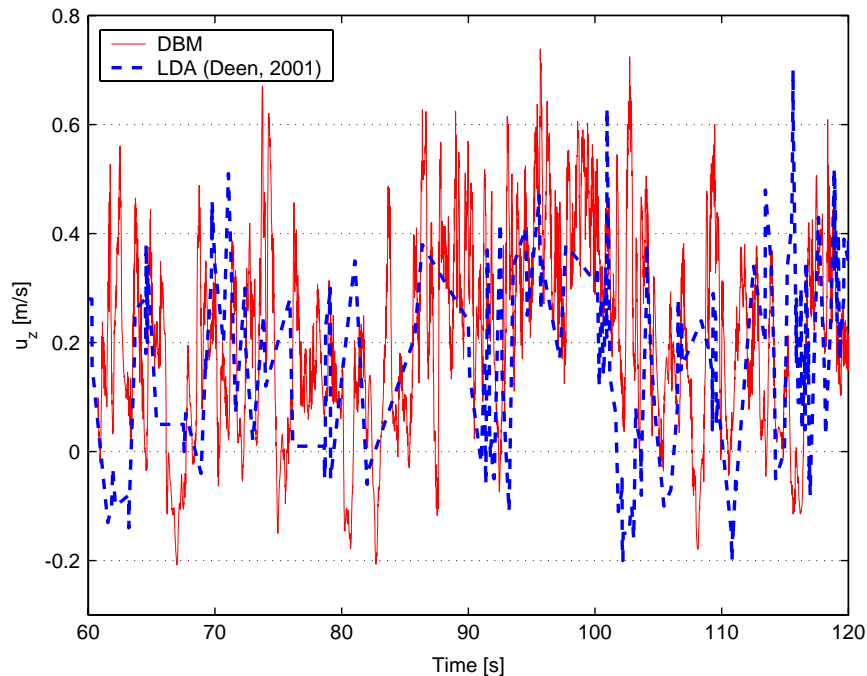
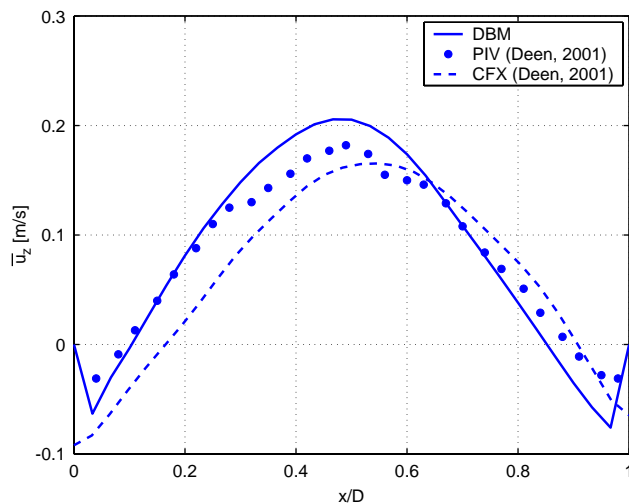Fig. 12. Time history of the vertical liquid velocity at the centerline of the column and at a height of $z/H = 0.56$.

Fig. 13. Comparison of simulated and experimental profiles of the liquid vertical average velocity ($\bar{u}_z$), at a height of $z/H = 0.56$ and a depth $y/W = 0.5$.

The mixing time is quantified by monitoring the mass fractions of the three tracers at the centerline axis, at a height of $z/H = 0.5$ (see Fig. 17). As can be seen from this figure, a homogeneous mixture is reached after 8 s. This figure also shows that the mass fraction is bounded between 0 and 1 and the sum of all species is conserved during the simulation.

6.3. Physical absorption

In this case study the physical absorption of CO_2 in water is simulated. CO_2 gas is fed into the column filled with water. A species transport equation is utilized to track the mass fractions of CO_2 in the liquid phase. Initially there is no dissolved CO_2 present in the column. During the process of the physical absorption, a relatively low mass transfer rate is experienced by the bubbles.

Fig. 18 shows the transient behavior in the column after the CO_2 bubbles are injected into the column. As can be seen, the hydrodynamics are relatively similar to the air–water case as described in the previous test cases. The size of the bubbles is only slightly changed during their presence in the column. A high fraction of dissolved CO_2 can be found in the vicinity of the bubbles. The dissolved CO_2 is convected by the liquid to other parts of the column.

The overall mass transfer rate can also be estimated by integrating Eq. (14) over the entire column. In the case of no mass transfer enhancement, this yields the following expression for the mean dissolved CO_2 concentration in the column at time t:

$$\frac{[CO_2(aq)](t)}{H[CO_2(g)]} = 1 - \exp \frac{-t N_b k_l A_b}{V_l} \tag{32}$$

with N_b the (averaged) total number of bubble and V_l the (averaged) liquid volume of the column. The mass transfer coefficient k_l is calculated using the theoretical terminal rise velocity as explained in Section 5 while the interfacial area A_b is calculated by assuming constant bubble size.

According to Eq. (32), the dissolved CO_2 is accumulated exponentially in time. The interphase mass transfer decreases as the dissolved CO_2 concentration increases and eventually diminished when the equilibrium condition as prescribed by the Henry constant is reached.
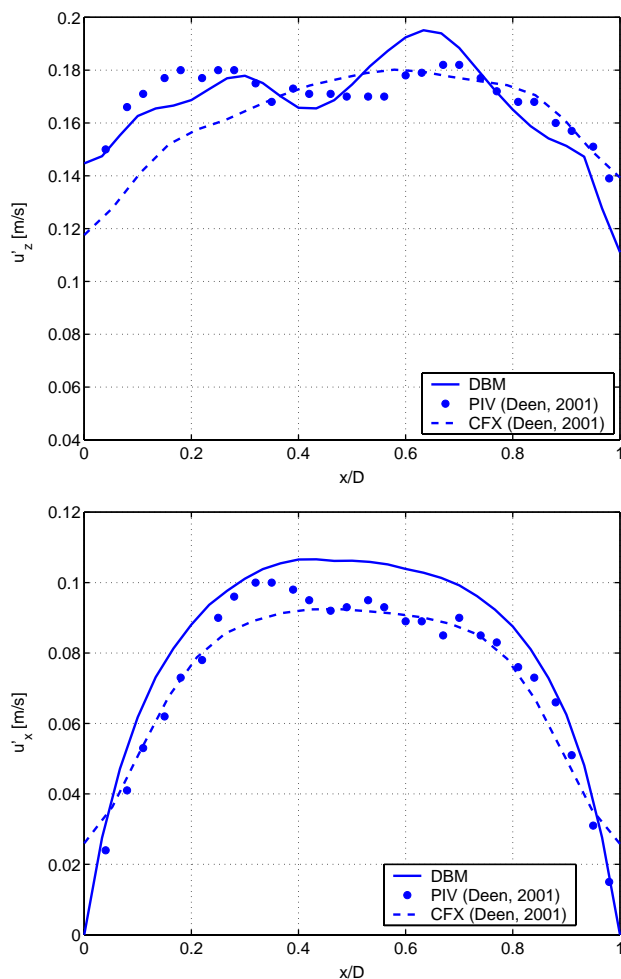
Fig. 14. Comparison of simulated and experimental profiles of the liquid velocity fluctuations, at a height of $z/H = 0.56$ and a depth $y/W = 0.5$. Top: vertical fluctuations (u'_z), bottom: horizontal fluctuations (u'_x).
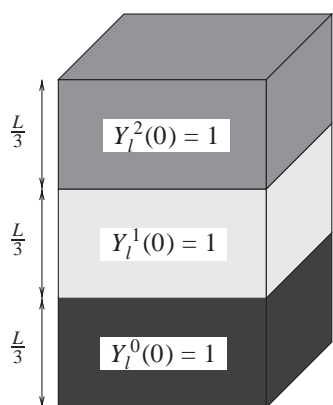

Fig. 15. Initial condition used for the mixing study. The column is divided into three different regions. Only one species is initially present in each region.

Fig. 19 shows the concentration of CO_2 at the centerline of the column, at a height of $z/H = 0.5$ resulting from the DBM simulation compared with the macro balance calcula-

tion given by Eq. (32) within the time interval 0–500 s. As can be seen in this figure, the macro balance shows good agreement with the DBM results. The discrepancy observed is less than 5%, which might come from the fact that DBM employs the exact number of bubbles as well as the bubbles and liquid properties in calculating the mass transfer, in contrast with the average value and constant size used in the macro balance model. Furthermore, in the macro balance model it is assumed that the transferred components are ideally mixed in the liquid, which is in contrast to the findings of the DBM.

6.4. Bubble column under reactive conditions

In this case study, we combine all the models described in Section 2 to obtain a complete, comprehensive model for a bubble column under reactive conditions. The chemisorption of CO_2 into aqueous NaOH solution is chosen as a test case, since it accounts for important phenomena that are encountered in practice.

The reaction mechanism of the chemisorption of carbon dioxide in an aqueous solution of sodium hydroxide is well understood and the reaction kinetics are well documented. The reaction sequence comprises several steps, which are given below

$$CO_2(g) \longrightarrow CO_2(aq), \tag{33}$$

$$CO_2(aq) + OH^- \rightleftharpoons HCO_3^-, \tag{34}$$

$$HCO_3^- + OH^- \rightleftharpoons CO_3^{2-} + H_2O. \tag{35}$$

At high pH the second reaction is considered to be instantaneous. Thus in the present study the overall reaction can be simplified into

$$CO_2(aq) + 2OH^- \rightleftharpoons CO_3^{2-} + H_2O. \tag{36}$$
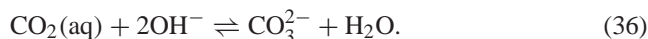
Since the first reaction is rate determining, the rate of the overall reaction is taken from the first reaction. The forward and backward reaction rate can, respectively, be formulated as

$$R_{1,1} = k_{1,1}[CO_2(aq)][OH^-], \tag{37}$$

$$R_{1,2} = k_{1,2}[HCO_3^-], \tag{38}$$

where $k_{1,1}$ and $k_{1,2}$ are the forward and backward reaction rate constants, respectively.

The influence of the chemical reaction on the gas absorption process is usually accounted for by an enhancement factor, E. This factor can be calculated numerically by solving the (coupled) diffusion equations in the boundary layer surrounding the bubbles. The equations should be solved for each individual bubble, hence in the case where a large number of bubbles is present this method becomes impractical. In the present study, an approximate solution of the enhancement factor is used. The enhancement factor takes a simple algebraic form as a function of the Hatta number
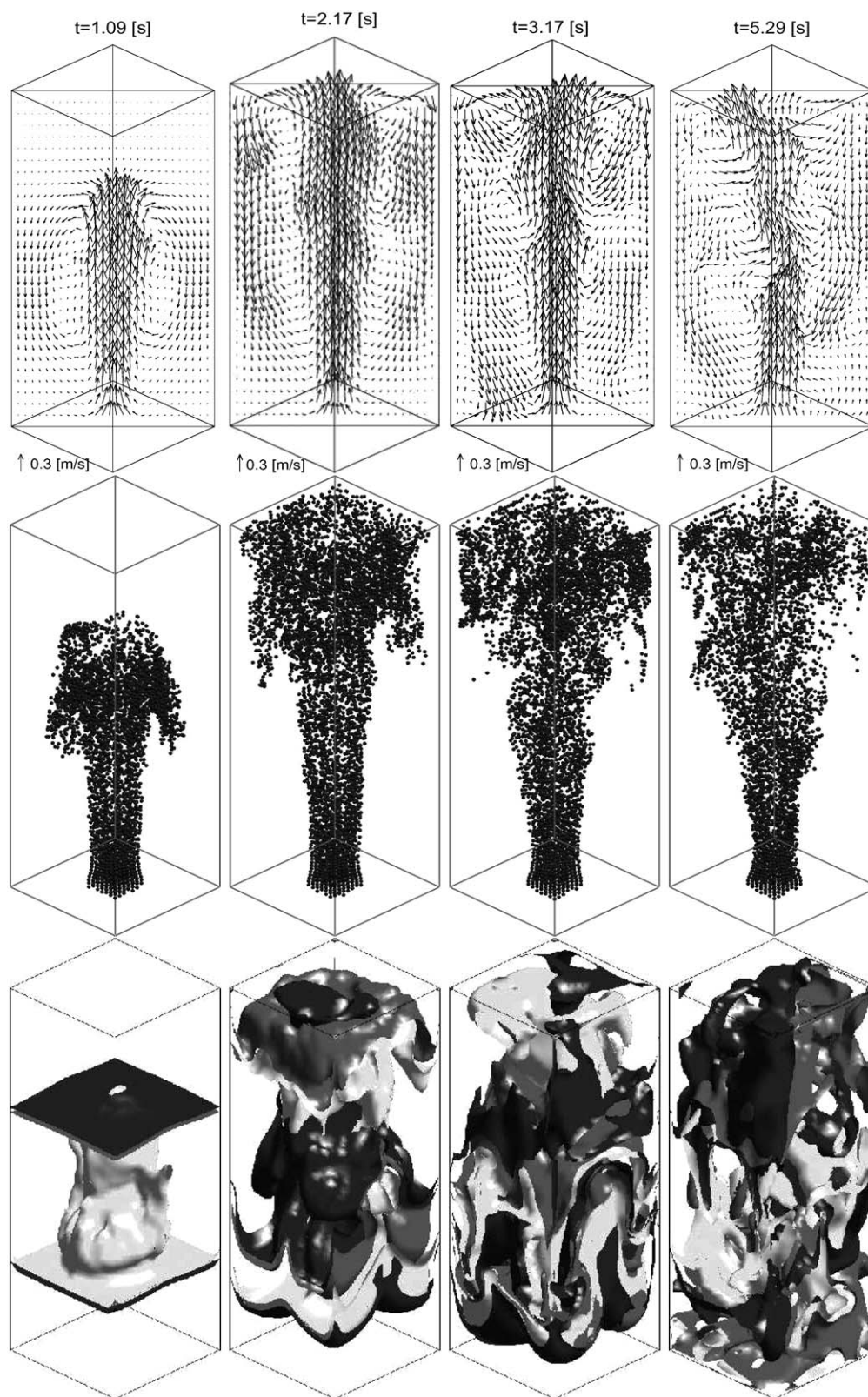
Fig. 16. Set of corresponding velocity fields (top), bubble position (middle) and isosurface of 30% tracer mass fraction (bottom) obtained from simulation of air–water bubble column with additional three passive scalar act as tracer at different time after the air was switched on. Gas superficial velocity = 4.9 mm/s.
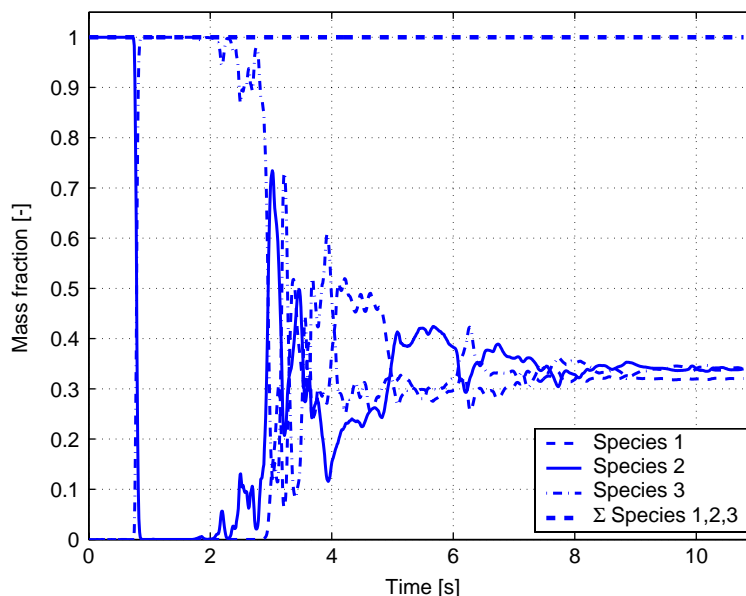
Fig. 17. Variation of the tracer during the mixing sequence at the centerline of the column and at a height of $z/H = 0.5$.

(Westerterp et al., 1998)

$$E = \begin{cases} -\frac{Ha^2}{2(E_\infty - 1)} \\ +\sqrt{\frac{Ha^4}{4(E_\infty - 1)^2} + E_\infty \frac{Ha^2}{E_\infty - 1} + 1}; & E_\infty > 1, \\ 1; & E_\infty \leqslant 1, \end{cases} \quad (39)$$

where

$$E_\infty = \left(1 + \frac{D_{OH^-}[OH^-]}{2D_{CO_2}H[CO_2(g)]}\right)\sqrt{\frac{D_{CO_2}}{D_{OH^-}}}, \quad (40)$$

$$Ha = \frac{\sqrt{k_{1,1}D_{CO_2}[OH^-]}}{k_l}. \quad (41)$$

This approach provides a much cheaper solution for the enhancement factor for each individual bubble. The variation of the enhancement factor, E, for pH ranging from 7 to 14 can be seen in Fig. 20. As we can see the physical mass transfer rate is significantly enhanced by the chemical reaction at pH > 12. Compared to the detailed simulation result using the two-film model by Fleischer et al. (1996), the approximate relation can represent the enhancement factor quite well. Small discrepancy is observed at high pH range. However, since this is only a test case to demonstrate the capabilities of the E–L model, the approximate relation for the enhancement factor given by Eq. (39) is considered to be adequate to describe the physical phenomena.

During the chemisorption process, due to the high interphase mass transfer rate, it is possible that bubbles are completely dissolved in the liquid. In our model a bubble is considered to be completely dissolved in the liquid when the bubble radius is less than 1 μm, while the bubble growth rate is negative (i.e. the bubble is still dissolving). If a bubble

meets this criteria, it will be disposed from the column and no longer being tracked.

The chemisorption problem is simulated using the DBM model. CO_2 gas is fed into the column filled with NaOH solution with an initial pH of 14. Three species transport equation are utilized to track mass fractions of $CO_2(aq)$, OH^- and CO_3^{2-}. A summary of the initial conditions and the source terms used in each transport equation is presented in Table 3.

Fig. 21 shows the transient behavior in the column immediately after the CO_2 bubbles are injected into the column. Shortly after bubbles are released into the column, a typical mushroom like shape appears. This shape is however, less pronounced compared to the case without absorption as described in Section 6.1. Due to the chemically enhanced mass transfer, the bubbles are completely dissolved within 0.15 m from the bottom and remain in that position for quite a while. Although the bubbles only appear in the lower part of the column, the liquid circulation induced by the bubbles extends to the top portion of the column. Compared to the case without absorption, the liquid phase oscillation is only observed in the higher part of the column. Since no bubbles are present in this region, these oscillations do not interact with bubbles, which makes them less pronounced.

Fig. 22 shows the transient behavior of chemical species distribution in the column. Since bubbles are only present in the lower part of the column, the mass transfer and reactions only take place close to the gas inlet. CO_2 gas, which dissolves into the liquid from the bubbles immediately reacts with hydroxide to produce carbonate, hence only very small traces of dissolved CO_2 can be found in the vicinity of the bubbles. The hydroxide ions that have been consumed by the reaction as well as the newly formed carbonate ions
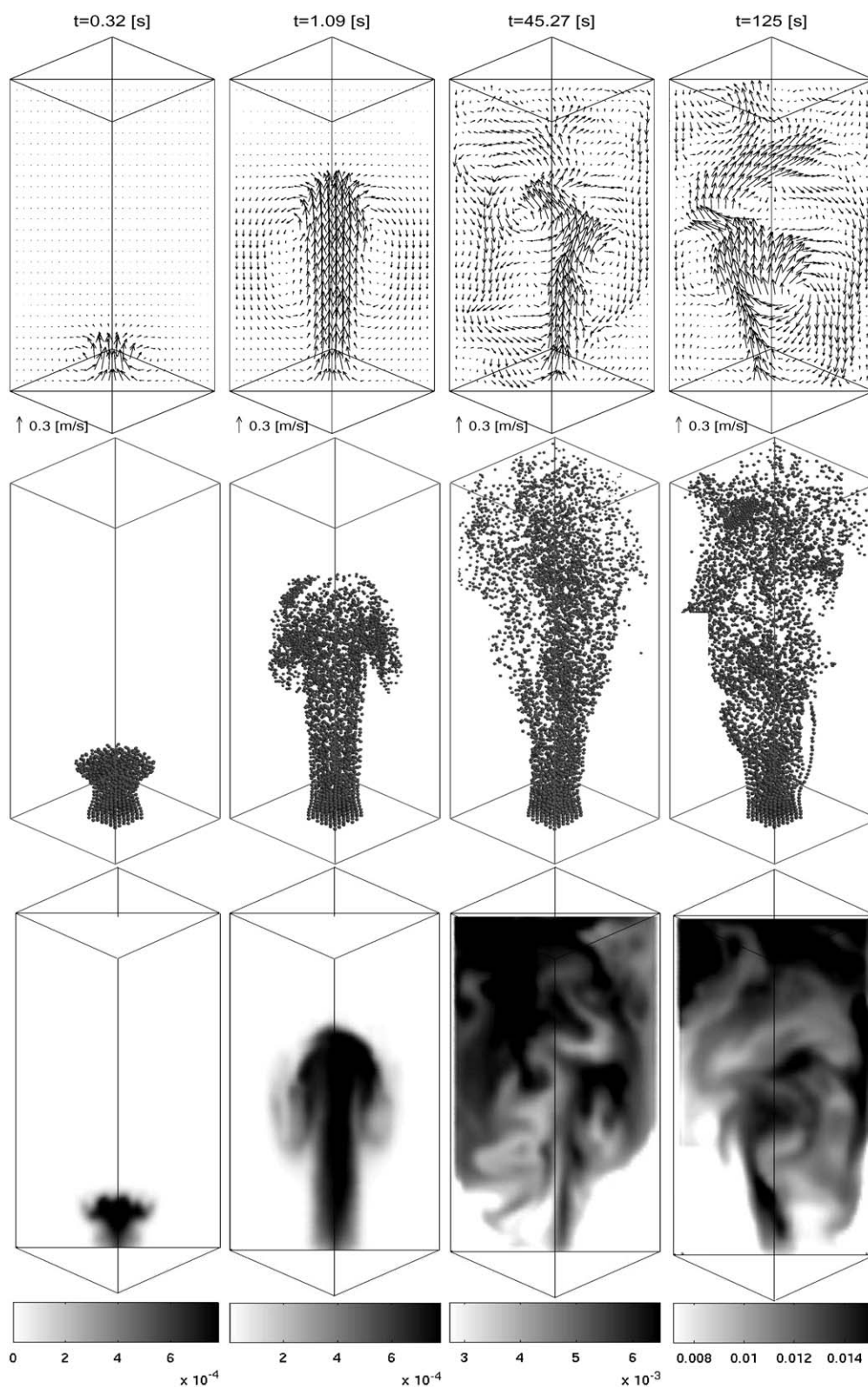
Fig. 18. Set of corresponding velocity fields (top), bubble position (middle) and distribution of dissolved CO_2 concentration (mol/l) (bottom) obtained from simulation of the physical absorption of CO_2 gas in water at various time after the CO_2 gas was switched on. CO_2 gas superficial velocity $= 4.9$ mm/s.
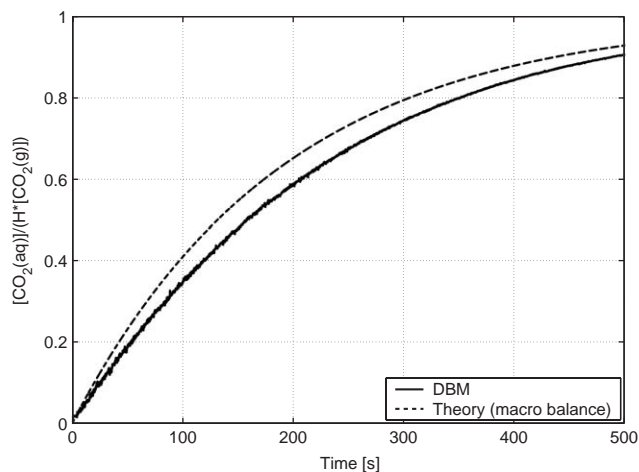
Fig. 19. Normalized dissolved CO_2 concentration at the centerline of the column and at a height of $z/H = 0.5$ compared with macro balance model. Simulation result of physical absorption of CO_2 bubbles in water. CO_2 gas superficial velocity $= 4.9$ mm/s. $N_b = 4643$.
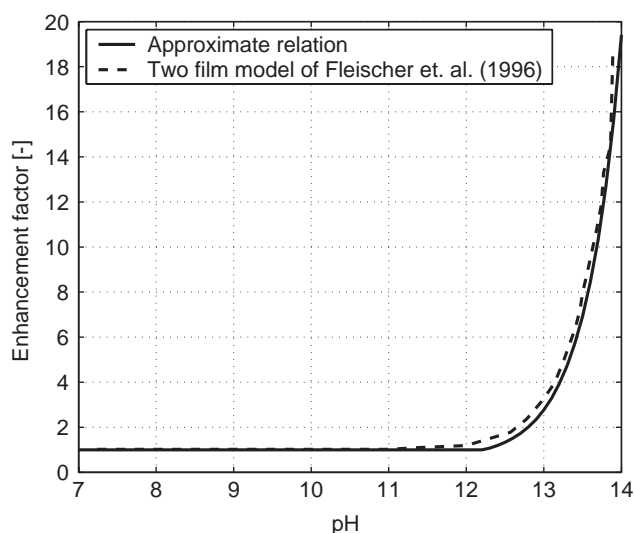

Fig. 20. pH-dependence of the enhancement factor E determined using approximate relation compared with the detailed simulation with the two-film model of Fleischer et al. (1996).

Table 3
Initial conditions and source terms used in the species transport equations

j	Species	$Y_l^j (t = 0)$	S^j / M_w^j (kmol/m^3 s)
0	$CO_2(aq)$	1×10^{-50}	$-R_{1,1} + R_{1,2}$
1	OH^-	$Y_1(pH)$	$2(-R_{1,1} + R_{1,2})$
2	CO_3^{2-}	1×10^{-50}	$R_{1,1} - R_{1,2}$

served by Fleischer et al. (1996). To investigate whether our model is capable to predict such behavior, a series of simulations with an initial pH varying from 13 up to 14 has been conducted. This technique is used to save calculation time, since the rate of change of pH is very low. Fig. 23 shows that the aforementioned behavior is nicely predicted by the current model. As the pH decreases the position where bubbles are completely dissolved moves upward and since the model is also able to predict the decrease of pH in time we can conclude that this behavior can also be captured if we would proceed the simulation for a sufficiently long period.

7. Conclusions

A model that combines hydrodynamics, mass transfer and chemical reaction in a bubble column has been successfully formulated and implemented. The simulation results obtained shows that the model can be used to investigate those phenomena in more detail than before.

Simulation of a single rising bubble in a quiescent liquid shows that the model is able to predict the terminal rise velocity correctly. In combination with a constant mass transfer rate, the model also accurately produces the bubble size as a function of time.

The hydrodynamics model has been validated using the experimental data of Deen et al. (2001). Both instantaneous and time-averaged liquid velocities predicted by the model are in good agreement with the experimental data. The experimentally observed meandering of the bubble plume is also nicely predicted by the present model.

By combining the hydrodynamics and chemical species transport equations, the mixing mechanism in the column can be studied in more detail. Our simulations indicate that intense mixing prevails at regions where sudden changes in flow direction occur.

One of the key features of the model presented in this paper is its capability to track individual bubbles in time. By calculating the mass transfer rate for each individual bubble and combining this information with a chemical species transport equation, gas absorption in reactive liquids can be described.

In the case of the physical absorption of CO_2 bubbles in water, it was found that the distribution of dissolved CO_2 is not uniform. Relatively high dissolved CO_2 was found in the vicinity of bubbles. In time the dissolved CO_2 is accumulated in the water until the equilibrium is attained. This

will be transported by the circulation flow to the top of the column in the center region and return back again through the downflow zone close to the column walls. This behavior suggests that the reactions taking place in the bottom part of the column are always supplied with relatively fresh reactant, since the product of the reaction is immediately transported by the liquid flow.

With time, the pH is decreasing and the carbonate concentration is continuously increasing. As the pH decreases, the enhancement factor, as shown in Fig. 20, also decreases, resulting in a lower mass transfer rate. In time the position where the bubbles are completely dissolved will slowly move upward. This behavior has been experimentally ob-
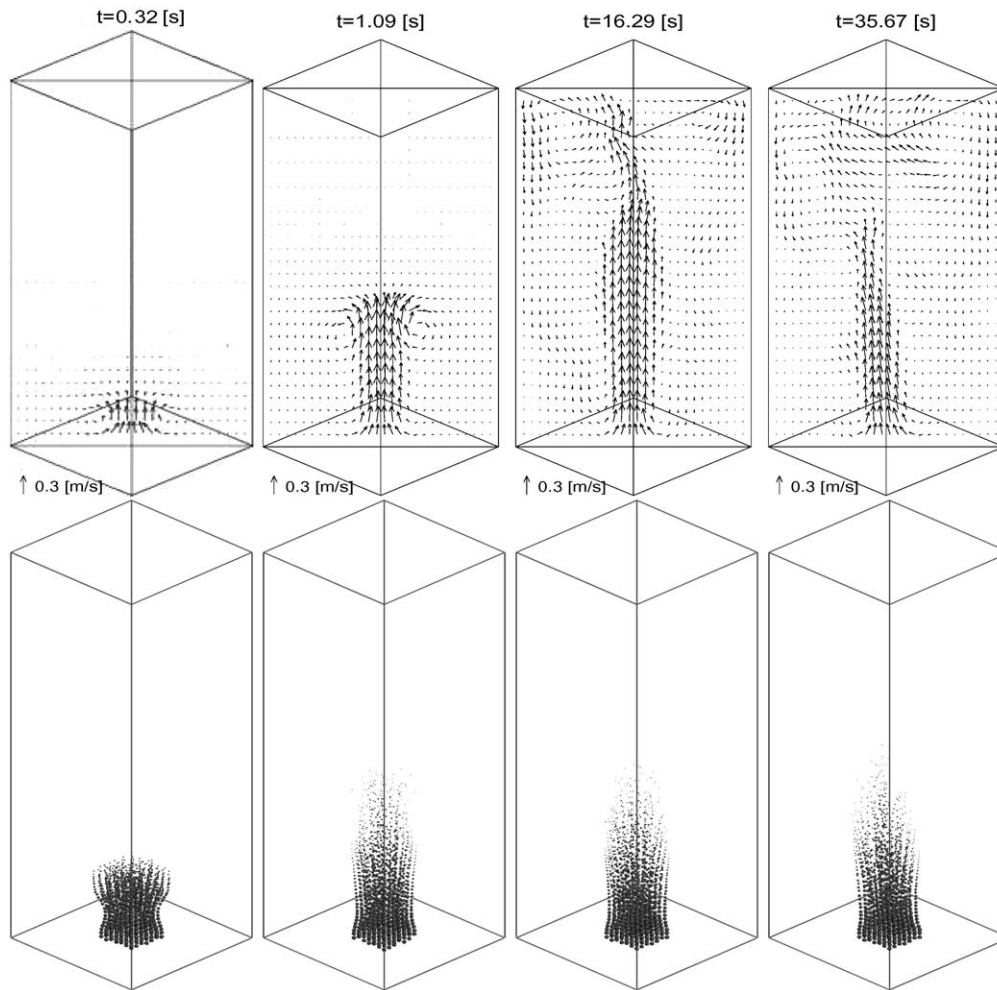
Fig. 21. Set of corresponding velocity fields (top), bubble position (bottom) obtained from simulation of the chemisorption of CO_2 gas in liquid NaOH at various time after the CO_2 gas was switched on. Initial NaOH pH = 14, CO_2 gas superficial velocity = 4.9 mm/s.

behavior shows good agreement compared with theoretical calculations.

The model was also used to investigate the chemisorption of CO_2 gas in NaOH solution. This process has been studied experimentally by Fleischer et al. (1996). The model is able to reveal liquid phase hydrodynamics, bubble size and position as well as chemical species distribution involves in the reaction. In simulations with initial pH = 14, bubbles are only present close to the gas inlet. Only very small traces of dissolved CO_2 can be found in the vicinity of the bubbles while the hydroxide ion that have been consumed and newly formed carbonate ions are transported through all the column region. In time the pH is decreasing while the carbonate ions is increasing. The model is also able to predict the position of completely dissolved bubbles due to chemically enhanced mass transfer. Variation of initial pH shows that this position shifts upward in the column as the pH decreases.

Due to the complexity and detailed information that the present model provides, calculation time is still the bottle-

neck especially for problems which involve a large number of bubbles and chemical species. In the current work, coalescence and break up were not considered. However, appropriate coalescence and break up models can readily be implemented due to the Lagrangian treatment of the bubble phase.

Notation

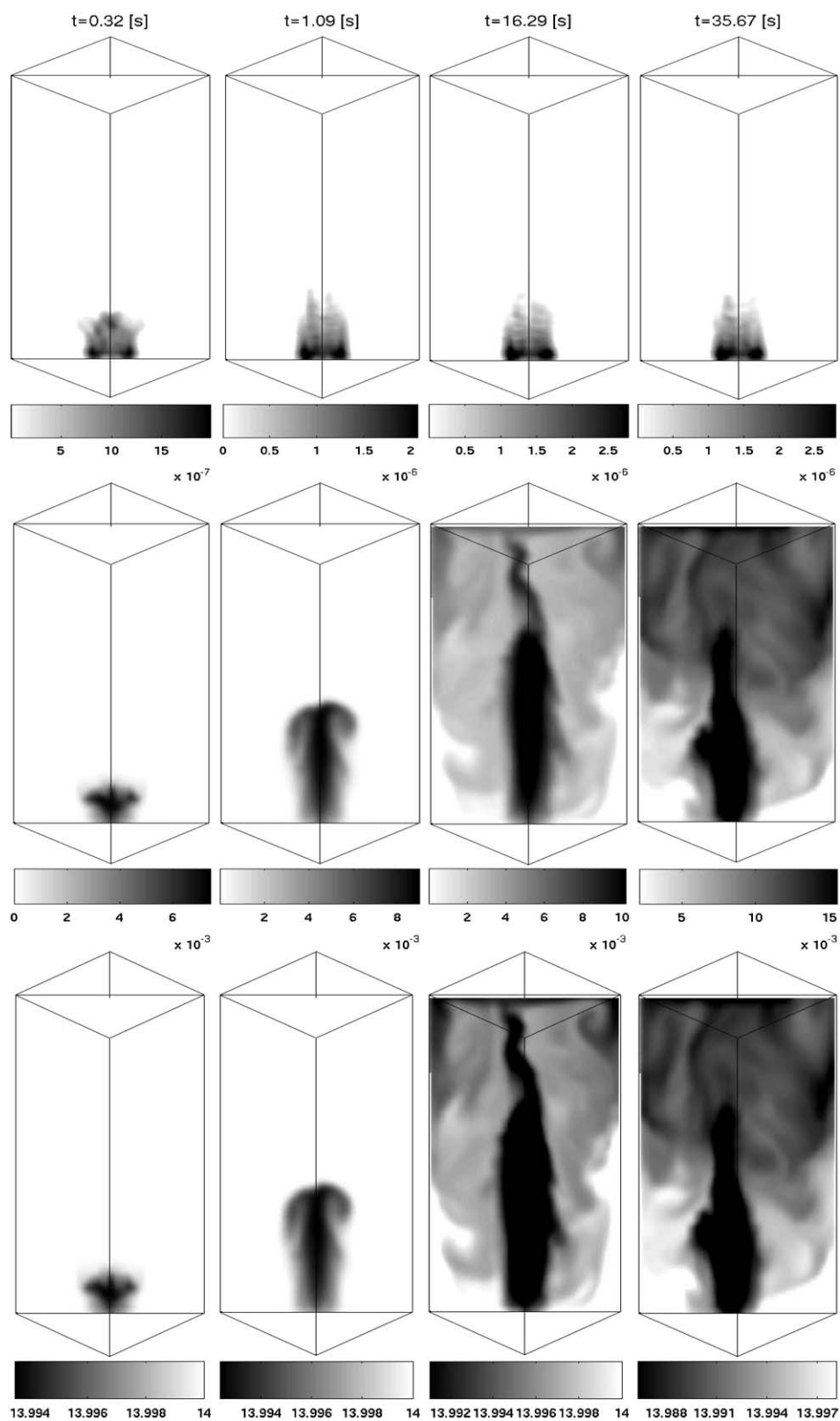|	
A	interfacial area, m^2
C	model coefficient, dimensionless
d	diameter, m
D	diffusivity $[m^2\,s^{-1}]$, depth, m
E	enhancement factor, dimensionless
$E\ddot{o}$	Eötvös number, $E\ddot{o} = (\rho_l - \rho_b)\mathbf{g}d_b^2/\sigma$, dimensionless
$\mathbf{F}$	force vector, N
$\mathbf{g}$	gravity acceleration, $m\,s^{-2}$

Fig. 22. Set of corresponding dissolved CO_2 concentration (mol/l) (top), CO_3^{2-} concentration (mol/l) (middle) and liquid phase pH [−] (bottom) obtained from simulation of the chemisorption of CO_2 gas in liquid NaOH at various time after the CO_2 gas was switched on. $pH_0 = 14$; pure CO_2 gas superficial velocity $= 4.9$ (mm/s).
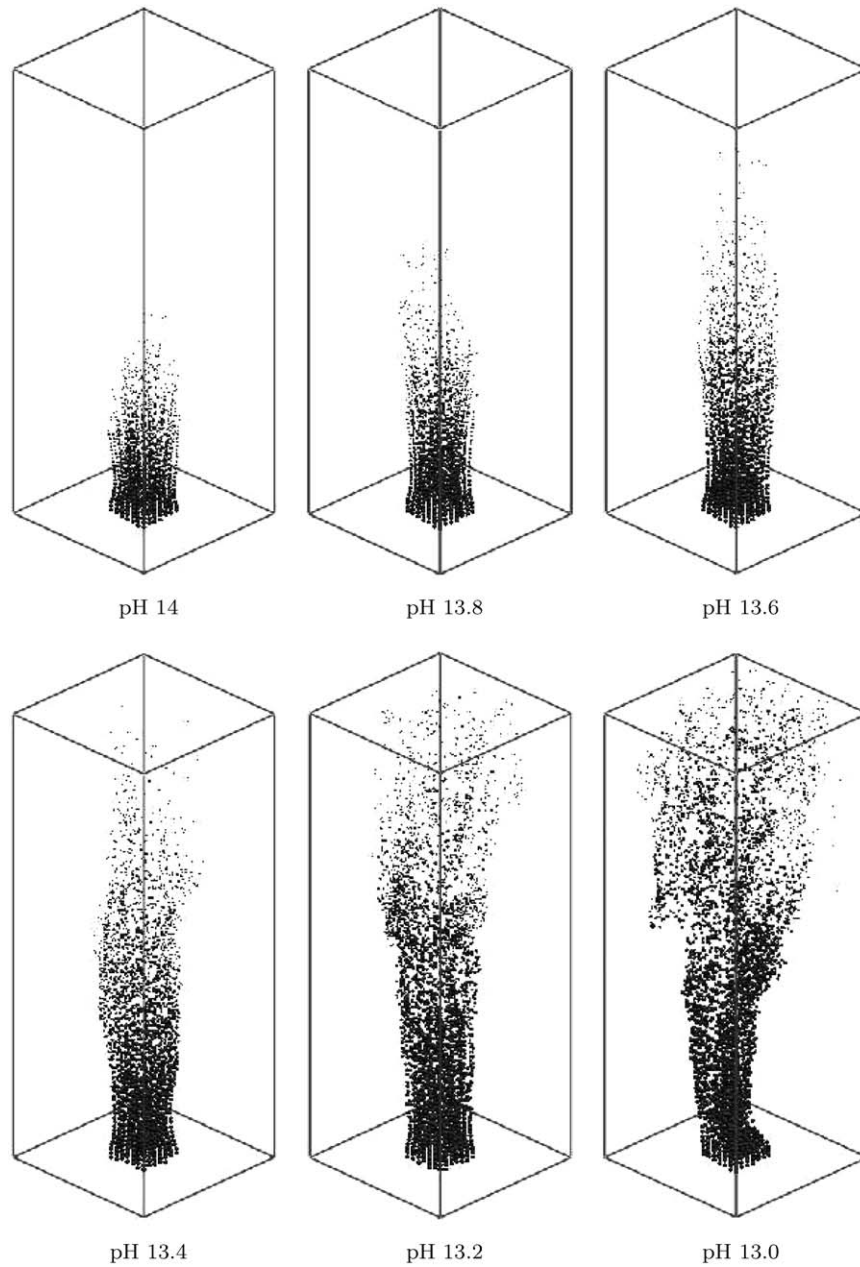
Fig. 23. Snapshot of bubble position at time $t = 10\,\text{s}$ after the CO_2 gas was switched on with variation of initial liquid NaOH pH. CO_2 gas superficial velocity $= 4.9\,(\text{mm/s})$.

H	Henry constant (aqueous-concentration/gas-concentration), dimensionless	
Ha	Hatta number, dimensionless	
$k_{1,1}$	forward reaction rate constant, $\text{m}^3\,\text{kmol}^{-1}\,\text{s}^{-1}$	
$k_{1,2}$	backward reaction rate constant, s^{-1}	
k_l	mass transfer coefficient, $\text{m}\,\text{s}^{-1}$	
$\mathbf{I}$	unit tensor, dimensionless	
m	mass, kg	
$\dot{m}$	mass transfer from individual bubble, $\text{kg}\,\text{s}^{-1}$	
$\dot{M}$	liquid side volume averaged mass transfer, $\text{kg}\,\text{s}^{-1}\,\text{m}^{-3}$	

M_w	molecular weight, $\text{kg}\,\text{kmol}^{-1}$
P	pressure, $\text{N}\,\text{m}^{-2}$
R	radius, m, reaction rate, $\text{kmol}\,\text{m}^{-3}\,\text{s}^{-1}$
Re	Reynolds number, $Re = \rho_l\,|\mathbf{v} - \mathbf{u}|\,d_b/\mu_l$, dimensionless
S	source term in the species balance equation, $\text{kg}\,\text{m}^{-3}\,\text{s}^{-1}$
$\mathbf{S}$	characteristic filtered strain rate, s^{-1}
Sc	Schmidt number, $Sc = \mu_l/(\rho_l D)$, dimensionless
Sh	Sherwood number, $Sh = k_l d_b/D$, dimensionless
t	time, s

$\mathbf{u}$	liquid velocity vector, m s^{-1}
$\bar{\mathbf{u}}$	liquid mean velocity, m s^{-1}
$\mathbf{u}'$	liquid velocity fluctuation vector, m s^{-1}
$\mathbf{v}$	bubble velocity vector, m s^{-1}
V	volume, m^3
W	width, m
Y	mass fraction, dimensionless
$[.]$	concentration, kmol m^{-3}

Greek letters

Γ	species diffusion coefficient, m^2 s^{-1}
δ_b	distance between two consecutive bubble, m
$\triangle$	subgrid length scale, m
ε	volume fraction, dimensionless
ζ	volume fraction of a bubble included in a cell, dimensionless
μ	viscosity, kg m^{-1} s^{-1}
ρ	density, kg m^{-3}
σ	interfacial tension, N m^{-1}
τ	stress tensor, N m^{-2}
Φ	volume averaged momentum transfer due to interphase forces, N m^{-3}
ω	Lagrangian quantity
Ω	Eulerian quantity

Indices

aq	aqueous
b	bubble
cell	computational cell
D	drag
eff	effective
G	gravity
j	jth species
l	liquid
L	lift
P	pressure
s	superficial
S	subgrid
T	turbulent
VM	virtual mass
$*$	interfacial equilibrium value

Acknowledgements

References

Al-Rashed, M.H., Jones, A.G., 1999. CFD modelling of gas–liquid reactive precipitation. Chemical Engineering Science 54, 4779–4784.

Allen, M.P., Tildesley, D.J., 1987. Computer Simulation of Liquids. Oxford Science Publications, Oxford.

Balay, S., Buschelman, K., Gropp, W.D., Kaushik, D., Knepley, M., McInnes, L.C., Smith, B.F., Zhang, H., 2001. PETSc home page. http://www.mcs.anl.gov/petsc.

Becker, S., Sokolichin, A., Eigenberger, G., 1994. Gas–liquid flow in bubble columns and loop reactors: Part II. Comparison of detailed experiments and flow simulations. Chemical Engineering Science 49, 5747–5762.

Bird, R.B., Stewart, W.E., Lightfoot, E.N., 2002. Transport Phenomena. second ed.. Wiley, New York.

Buwa, V.V., Ranade, V.V., 2002. Dynamics of gas–liquid flow in a rectangular bubble column: experimental and single/multi-group CFD simulations. Chemical Engineering Science 57, 4715–4736.

Centrella, J., Wilson, J.R., 1984. Planar numerical cosmology. II. The difference equations and numerical tests. Astronomy & Astrophysics Journal Supplement Series 54, 229–249.

Cents, A.H.G., Brilman, D.W.F., Wijnstra, P.J., Regtien, P.P.L., Versteeg, G.F., 2003. Measurement of bubble, drop and particle size distribution in multi-phase systems using ultrasonic spectroscopy. Canadian Journal of Chemical Engineering.

Chen, R.C., Reese, J., Fan, L.S., 1994. Flow structure in a three-dimensional bubble column and three-dimensional fluidized bed. A.I.Ch.E. Journal 40, 1093–1104.

Deen, N.G., Solberg, T., Hjertager, B.H., 2001. Large eddy simulation of the gas–liquid flow in a square cross-sectioned bubble column. Chemical Engineering Science 56, 6341–6349.

Delnoij, E., Lammers, F.A., Kuipers, J.A.M., van Swaaij, W.P.M., 1997. Dynamic simulation of dispersed gas–liquid two-phase flow using a discrete bubble model. Chemical Engineering Science 52, 1429–1458.

Delnoij, E., Kuipers, J.A.M., van Swaaij, W.P.M., 1999. A three-dimensional CFD model for gas–liquid bubble columns. Chemical Engineering Science 54, 2217–2226.

Ferziger, J.H., Peric, M., 1999. Computational Methods for Fluid Dynamics. Springer, Berlin.

Fleischer, C., Becker, S., Eigenberger, G., 1996. Detailed modeling of the chemisorption of CO$_2$ into NaOH in a bubble column. Chemical Engineering Science 51, 1715–1724.

Hjertager, B.H., 1998. Computational fluid dynamics (CFD) analysis of multiphase chemical reactors. Trends in Chemical Engineering 4, 44–92.

Hoomans, B.P.B., Kuipers, J.A.M., Briels, W.J., Swaaij, W.P.M.V., 1996. Discrete particle simulation of bubble and slug formation in a two-dimensional gas-fluidised bed: a hard-sphere approach. Chemical Engineering Science 51 (1), 99–118.

Kuipers, J.A.M., van Duin, K.J., van Beckum, F.P.H., van Swaaij, W.P.M., 1993. Computer simulation of the hydrodynamics of a two dimensional gas-fluidized bed. Computational Chemical Engineering 17, 839.

Láin, S., Sommerfeld, M., 2004. LES of gas–liquid flow in a cylindrical laboratory bubble column. Yokohama, Japan. 5th International Conference on Multiphase Flow, ICMF'04. Paper no. 337.

Márquez, M.A., Amend, R.J., Carbonell, R.G., Sáez, A.E., Roberts, G.W., 1999a. Hydrodynamics of gas-lift reactors with a fast, liquid-phase reaction. Chemical Engineering Science 54, 2263–2271.

Márquez, M.A., Sáez, A.E., Carbonell, R.G., Roberts, G.W., 1999b. Coupling of hydrodynamics and chemical reaction in gas-lift reactors. A.I.Ch.E. Journal 45 (2), 410–423.

Pan, Y., Dudukovic, M.P., 2000. Numerical investigation of gas-driven flow in 2-d bubble columns. A.I.Ch.E. Journal 46, 434–449.

Ranade, V.V., Tayalia, Y., 2001. Modelling of fluid dynamics and mixing in shallow bubble column reactors: influence of sparge design. Chemical Engineering Science 56, 1667–1675.

Smagorinsky, J., 1963. General circulation experiment with the primitive equations. Monthly Weather Review 91, 99–165.

Sokolichin, A., Eigenberger, G., 1994. Gas–liquid flow in bubble columns and loop reactors: Part i. Detailed modelling and numerical simulation. Chemical Engineering Science 49, 5735–5746.

Tomiyama, A., Zun, I., Higaki, H., Makino, Y., Sakaguchi, T., 1997. A three-dimensional particle tracking method for bubble flow simulation. Nuclear Engineering and Design 175, 77–86.

van den Hengel, E.I.V., Darmana, D., Deen, N.G., Kuipers, J.A.M., 2003. Large eddy simulation of a bubble column reactor using the Euler–Lagrange approach. Computational Fluid Dynamics in Chemical Reaction Engineering III, Davos, Switzerland.

Westerterp, K.R., van Swaaij, W.P.M., Beenackers, A.A.C.M., 1998. Chemical Reactor Design and Operation. Wiley, New York.